



HHS Public Access

Author manuscript

Cell Rep. Author manuscript; available in PMC 2021 November 04.

Published in final edited form as:

Cell Rep. 2021 October 12; 37(2): 109827. doi:10.1016/j.celrep.2021.109827.

The endocycle restores tissue tension in the *Drosophila* abdomen post wound repair

Vicki P. Losick^{1,2,*}, Levi G. Duhaime¹

¹Biology Department, Boston College, Chestnut Hill, MA 02467, USA

²Lead contact

SUMMARY

Polyploidy frequently arises in response to injury, aging, and disease. Despite its prevalence, major gaps exist in our understanding of how polyploid cells alter tissue function. In the adult *Drosophila* epithelium, wound healing is dependent on the generation of multinucleated polyploid cells resulting in a permanent change in the epithelial architecture. Here, we study how the wound-induced polyploid cells affect tissue function by altering epithelial mechanics. The mechanosensor nonmuscle myosin II is activated and upregulated in wound-induced polyploid cells and persists after healing completes. Polyploidy enhances relative epithelial tension, which is dependent on the endocycle and not cell fusion post injury. Remarkably, the enhanced epithelial tension mimics the relative tension of the lateral muscle fibers, which are permanently severed by the injury. As a result, we found that the wound-induced polyploid cells remodel the epithelium to maintain fly abdominal movements, which may help compensate for lost tissue tension.

Graphical Abstract

This is an open access article under the CC BY-NC-ND license (<http://creativecommons.org/licenses/by-nc-nd/4.0/>).

*Correspondence: vicki.losick@bc.edu.

AUTHOR CONTRIBUTIONS

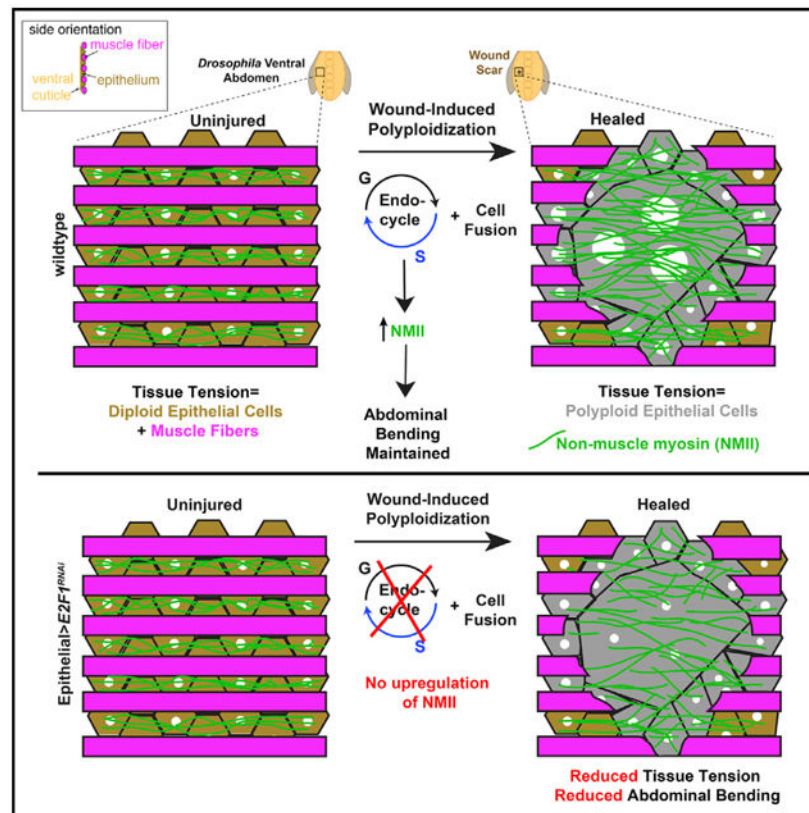
Conceptualization, V.P.L.; methodology, L.G.D. and V.P.L.; validation, L.G.D. and V.P.L.; formal analysis, L.G.D. and V.P.L.; investigation, L.G.D. and V.P.L.; resources, L.G.D. and V.P.L.; data curation, L.G.D. and V.P.L.; writing – original draft, V.P.L.; writing – review & editing, L.G.D. and V.P.L.; visualization, L.G.D. and V.P.L.; project administration, V.P.L.; supervision, V.P.L.; funding acquisition, V.P.L.

SUPPLEMENTAL INFORMATION

Supplemental information can be found online at <https://doi.org/10.1016/j.celrep.2021.109827>.

DECLARATION OF INTERESTS

The authors declare no competing interests.



In brief

Losick and Duhaime show that the generation of polyploid cells by the endocycle induces myosin expression resulting in enhanced epithelial tension after wound repair. This change in epithelial mechanics appears to compensate for the permanent loss of muscle fibers, which is necessary for efficient abdominal bending in the fruit fly.

INTRODUCTION

Polyploidy is the more than doubling of a cell's genome and is a widespread mechanism of cellular growth and adaptation. Cells become polyploid by cell fusion or endoreplication, which encompasses two variant cell cycles: endocycle and endomitosis. The endocycle bypasses M phase with successive S and G phases that double the genome size with each cycle, whereas M phase is truncated in endomitosis, resulting in a mono- or binucleated cell (Gjelsvik et al., 2019). Endoreplication allows cells to grow exponentially, since cell size scales with ploidy, and DNA content is known as the C-value (Frawley and Orr-Weaver, 2015). Polyploidy therefore permits the growth of many cell types (e.g., muscle, epithelial, and endothelial cells), organs/tissues, and organisms (Fox and Duronio, 2013; Orr-Weaver, 2015).

Recent discoveries have revealed that polyploidy can pose either an adaptive advantage or disadvantage to the organism depending on the context, but it is often selected for under conditions of stress. For plants, enhanced polyploidy promotes resistance against

environmental insults, including salinity (Qi and Zhang, 2020). In fungi, polyploidy enhances the pathogenesis of *Candida albicans* and confers its drug resistance (Harrison et al., 2014; Todd et al., 2017). Polyploidy also provides resilience to environmental insults in *Saccharomyces cerevisiae* (Storchova, 2014). In the liver, polyploidy can make hepatocytes more resistant to tumor growth by reducing proliferation (Wilkinson et al., 2019; Zhang et al., 2018). In contrast, polyploidy in the tetraploid state predisposes mouse mammary epithelial cells to aneuploidy, resulting in tumorigenesis (Fujiwara et al., 2005; Shu et al., 2018). In the heart, cardiomyocyte polyploidy impairs heart regeneration in both zebrafish and mouse models (González-Rosa et al., 2018; Han et al., 2020; Patterson et al., 2017). Therefore, depending on the context, polyploidy can be beneficial or detrimental to the survival of cells and organisms.

The growth of polyploid cells provides a healing advantage in many animal models (Gjelsvik et al., 2019; Lazzeri et al., 2019). Studies in fruit flies revealed that polyploidy is required for wound repair in the adult abdominal epithelium and hindgut pylorus (Losick et al., 2013). Polyploid cell growth compensates for cell loss by increasing cell size instead of cell number. More recent studies in these *Drosophila* tissues have revealed that polyploidy permits wound healing in the presence of genotoxic stress in the abdominal epithelium and is necessary to protect against oncogenic growth in the hindgut pylorus (Cohen et al., 2018; Grendler et al., 2019). Polyploid cell growth is also required to repair the fly intestine following bacterial infection (Xiang et al., 2017). In vertebrate animals, like in fruit flies, recent studies have revealed that endoreplication occurs in the mouse kidney tubule epithelium, liver hepatocytes, and zebrafish epicardium after damage to promote tissue repair and maintain organ function (Cao et al., 2017; Lazzeri et al., 2018; Lin et al., 2020; Wilkinson et al., 2019; Zhang et al., 2018).

Several conserved signaling pathways have been identified in ploidy regulation, including the Insulin Receptor, epidermal growth factor receptor-Ras, c-Jun N-terminal kinase, and Hippo-Yki/Yap signal transduction pathways (Losick et al., 2013, 2016; Tamori and Deng, 2013; Xiang et al., 2017), and it has begun to be recognized that there are mechanical signals that govern polyploid growth as well. One biophysical cue recently linked to polyploid cell growth is tension. Enhanced tension at the wound leading edge promoted epicardial cell endoreplication during zebrafish heart regeneration (Cao et al., 2017). Higher traction forces in epicardial cells delayed closure of the cytokinetic ring, ultimately leading to cytokinesis failure and endomitosis (Uroz et al., 2019). In *Drosophila*, increased mechanical tension was also shown to regulate cell-to-cell fusion during muscle development (Kim et al., 2015). We recently showed that wound-induced polyploidization (WIP) in adult fly epithelium relies on integrin and focal adhesion kinase (Besen-McNally et al., 2021). Other biophysical forces, including shear stress, are required to induce polyploidization of megakaryocytes during maturation (Jiang et al., 2014). While it has been shown in these studies that mechanical forces can promote polyploid cell growth, it remains unknown how polyploid cells, in turn, affect tissue mechanics.

To answer this question, we used an adult *Drosophila* epithelial wound healing model in which a needle puncture wound through the cuticle induces the generation of a large multinucleated, polyploid cell at the site of injury (Losick et al., 2013). Polyploidy occurs

in this tissue by cell fusion and the endocycle, leading to a permanent change in epithelial organization. Here, we find that the wound-induced polyploid cells enhance relative tissue tension, compared to diploid cells, altering epithelial mechanics after wound repair. The enhanced epithelial tension is dependent on the endocycle, which leads to an ~2-fold upregulation of nonmuscle myosin II (NMII) expression. The altered epithelial mechanics appear to be a functional adaptation to damage, as the underlying abdominal muscle fibers are severed as a result of injury and not repaired (Losick et al., 2013). By imaging *Drosophila* abdominal movements, we discovered that WIP functions to maintain efficient abdominal bending in male flies. Taken together, our study has uncovered an unexpected mechanism by which polyploidy allows the epithelium to adapt and alter its mechanics to help restore movement to the wounded fly abdomen.

RESULTS

Myosin is upregulated and persists in wound-induced polyploid cells

NMII is a key regulator of mechanotransduction and has been extensively studied in *Drosophila* embryogenesis and development (Heer and Martin, 2017). Myosin is a hexamer composed of two myosin heavy chains (HCs), two regulatory light chains (RLCs), and two essential light chains. In *Drosophila*, spaghetti squash (Sqh) encodes the RLC and zipper (Zip) encodes the HC (Lye and Sanson, 2011). To begin our study following NMII in the context of repair, we investigated the localization and expression of NMII in *Drosophila* adult abdominal epithelial cells to determine whether the actomyosin network is altered by WIP. We examined fly strains expressing either Sqh-GFP or Zip-GFP fusion proteins, and we discovered that both Sqh- and Zip-GFP fusion proteins were organized in a row-like pattern in the uninjured adult abdominal epithelium (Figures 1A and 1B). This is in part due to the surrounding abdominal muscle fibers, which dictate the shape and size of epithelial cells in the abdomen. The epithelial cells are the thickest in the spaces between the muscle fibers (Losick et al., 2013), which is also where Sqh-GFP intensity is the highest. After a puncture wound, the Sqh-GFP rows and lateral muscle fibers are disrupted and Sqh-GFP is reorganized into a meshwork appearance, losing the row-like pattern in the regions surrounding the wound site (Figures 1C–1E).

In many wound healing systems, myosin accumulates at the leading edge to facilitate directional cell migration and wound closure (Zulueta-Coarasa and Fernandez-Gonzalez, 2017). We did not observe an enrichment of Sqh-GFP at the leading edge but instead found that total Sqh-GFP expression was diffuse throughout the developing syncytium surrounding the wound site. We measured the average Sqh-GFP intensity in this area surrounding the wound scar and normalized it to the uninjured control to calculate the fold change. We found that there was no statistical difference in Sqh-GFP expression at 12 (Figure 1C), 18, or 24 h post injury (hpi) compared to the control (Figure 1F). By 30 hpi, Sqh-GFP fold change was significantly elevated surrounding the injury. This is when epithelial cells are undergoing WIP via the endocycle and cell fusion to form the multinucleated polyploid cells (Figure 1G). Peak induction of Sqh-GFP occurred at 36 hpi (2-fold on average) and persisted after wound closure completed at 72 hpi (Figures 1D–1G). The Sqh-GFP intensity broadened over the wound area, and the row-like organization was not restored in the area covering

the cuticle scar (W) and as shown in the corresponding plot profiles (Figures 1A''–1E''). This may be in part due to the permanent loss of overlaying abdominal muscle fibers in this area, which are severed by the puncture wound and not regenerated (Losick et al., 2013). As a control, we confirmed that the scar sizes were consistent at all times assayed, as the extent of WIP was previously shown to be dependent on the wound size (Figure 1H) (Losick et al., 2013). We also observed that the myosin HC, Zip-GFP localization was similarly reorganized and induced 1.7-fold at 96 hpi in healed polyploid epithelium as compared to uninjured diploid tissue (Figures 1I and 1J). Therefore, we found that the NMII network is permanently altered by injury even after wound closure completes.

The endocycle is required, but not sufficient, to enhance NMII expression and epithelial tension

The upregulation of myosin correlated with when the wound-induced polyploid cells are generated by the endocycle and fusion (Figures 1F and 1G) (Losick et al., 2013). To test this, we first measured the Sqh-GFP fold change to determine whether known WIP regulators alter NMII expression. Epithelial-specific knockdown of the endocycle regulators (*yki^{RNAi}*, *CycE^{RNAi}*, and *E2F1^{RNAi}*) strongly reduced Sqh-GFP to ~1.2-fold, whereas inhibition of cell fusion (*Rac^{DN}*) did not affect Sqh-GFP, which was still induced 2.3-fold at 3 dpi (Figures 2A, 2B, and S1A) (Losick et al., 2013, 2016). As expected, the syncytium still formed when the endocycle was inhibited, but the syncytium size was reduced by *Rac^{DN}*, which we previously showed interferes with cell fusion (Figure 2A) (Losick et al., 2013). This suggests that the endocycle is required for the induction of Sqh-GFP in the polyploid cells near the wound site and that fusion is dispensable.

Our previous study showed that overexpression of *Myc* is sufficient to drive the uninjured, postmitotic epithelial cells into the endocycle, boosting ploidy up to 16C (Grendler et al., 2019). By overexpressing *Myc*, we could then ask whether the endocycle is sufficient to enhance Sqh-GFP expression in the absence of injury. However, we found that the epithelial-specific expression of *Myc* did not upregulate Sqh-GFP (Figures 2C and 2D). Even at 3 dpi, when polyploidy is further enhanced by *Myc* overexpression (Grendler et al., 2019), Sqh-GFP intensity overlaying the wound scar was still ~2-fold, comparable to the control at 3 dpi (Figures S1B and S1C). This suggests that only in the context of a wound environment is the endocycle necessary for upregulation of Sqh-GFP.

An increase in NMII expression has been found to be indicative of enhanced epithelial tension, which is required for many tissue morphogenesis events during development (Heer and Martin, 2017). We therefore asked whether the enhanced Sqh expression results in altered epithelial mechanics in the fly wound-induced polyploid cells. To do so, we adapted a laser ablation approach and tested whether the relative epithelial tension in healed polyploid epithelial cells was significantly different from that of the uninjured, diploid epithelium. The relative initial recoil velocities were measured from time-lapse images taken before and after laser ablation of the Sqh-GFP network (Figure 2E and Video S1). We found that uninjured, diploid epithelium had an average initial recoil velocity (V_0) of 15.5 $\mu\text{m/s}$, whereas the healed (3 dpi) polyploid epithelium had an average V_0 of 38.3 $\mu\text{m/s}$ in

the Sqh-GFP localized adjacent to the wound site (Figures 2E and 2F and Video S1). This indicates that polyploid epithelium has a 2.47-fold increase in tension.

Next, we asked whether the enhanced epithelial tension was dependent on whether the polyploid cell growth arose by the endocycle using the *E2F1* knockdown (*E2F1^{RNAi}*) in uninjured and healed tissues (Figures 2E and 2F and Video S1). We found that V_0 in the *E2F1^{RNAi}* epithelium was significantly reduced by 2.5-fold at 3 dpi to 15.8 $\mu\text{m/s}$ (Figure 2F and Video S1). In addition, there was no significant difference in V_0 for the uninjured conditions (15.5 and 14.6 $\mu\text{m/s}$, respectively). Therefore, the endocycle is required to enhance epithelial tension in wound-induced polyploid cells. Likewise, V_0 for the laser-ablated *Myc* epithelium was not statistically different from the uninjured control (Figure 2H and Video S2). Therefore, the endocycle is required, but not sufficient, to enhance Sqh expression and epithelial tension post injury.

Diploid, but not polyploid, epithelial tension is dependent on NMII phosphorylation

Phosphorylation of NMIIRLC occurs at threonine-20 and serine-21 and in most systems activates myosin's motor activity cross-linking actin to generate mechanical forces within the cell (Vasquez et al., 2014). Using a phospho-specific myosin antibody (P-Myo), we observed P-Myo staining in uninjured epithelium in a similar row-like pattern as Sqh-GFP (Figure S2A). Likewise, at 3 dpi, P-Myo staining was upregulated 1.5-fold in wound-induced polyploid cells (Figures S2A and S2C). The Rho-associated kinase (Rok) is required for phosphorylation, and indeed we found that pharmacological inhibition of Rok significantly reduced P-Myo staining in the adult epithelium (Figures S2A–S2C). P-Myo staining was undetectable in both the uninjured and 3-dpi adult fly epithelium after treatment with a Rok inhibitor (γ -27632).

We next asked whether epithelial tension is dependent on NMII phosphorylation. Similarly, we found that epithelial tension was significantly higher in 3 dpi polyploid epithelium compared to uninjured, diploid epithelium (Figures 3A and 3B and Video S3). When myosin was pharmacologically inactivated by pre-treating the dissected abdominal tissue with the Rok inhibitor (γ -27632) just prior to laser ablation, we found that recoil velocity was significantly reduced compared to the buffer treatment alone. The Rok inhibitor reduced V_0 by 1.6- and 2.9-fold in uninjured and 3-dpi epithelium, respectively (Figures 3A and 3B and Video S3). Although the Rok inhibitor has been widely used to assay myosin activity, this drug is not specific for myosin phosphorylation and can also disrupt myosin filament assembly and myosin localization (Sellers et al., 1982; Uehata et al., 1997). To more specifically test the role of NMII phosphorylation in epithelial tension, we knocked down *Rok* (*Rok^{RNAi}*) with the epi-Gal4 driver (Figures S2D–S2F). Similar to a pharmacological Rok inhibitor, epithelial-specific *Rok^{RNAi}* also significantly reduced P-Myo staining, as it was undetectable in both the uninjured and 3 dpi epithelium. This demonstrated that the P-Myo staining was primarily in the epithelium and not in overlaying muscle fibers.

We then measured V_0 after laser ablation of the Sqh-GFP region in the uninjured epithelium and confirmed that tension is dependent on NMII phosphorylation, as *Rok^{RNAi}* reduced epithelial tension by 5.2-fold (Figures 3C and 3D). Surprisingly, we found that *Rok^{RNAi}* did not reduce epithelial recoil velocity at 3 dpi, which was comparable to the 3 dpi control.

In some cases, myosin motor activity has been found to be dispensable for actin network contractions, with myosin's role instead being to act as a crosslinker (Escuin et al., 2015; Ma et al., 2012; Sun et al., 2010). Indeed, we did observe that Sqh-GFP was upregulated 1.78-fold at 3 dpi even when *Rok* was knocked down (Figures 2B and S1A). Taken together, we found that polyploidy enhances epithelial tension, but tension in polyploid cells is independent of *Rok*.

Rok is not required for WIP

It was shown in zebrafish epicardium that tension is an activator of polyploid cell growth (Cao et al., 2017). NMII phosphorylation and actin stress fibers were observed in polyploid epicardial cells that arose at the wound leading edge. However, it was not determined whether NMII phosphorylation was necessary for polyploidy. Hence, we tested in our fly model whether *Rok* was required for WIP, either endocycle or cell fusion. First, we assayed whether the endocycle was perturbed by using our previously developed semi-automated method to quantify the distribution and ploidy of most nuclei throughout both the uninjured and repaired abdominal epithelium (Bailey et al., 2020; Losick et al., 2016). Immunofluorescence images of uninjured (–) and 3 dpi epithelium in control and *Rok^{RNAi}* flies were obtained with stains for epithelial nuclei (Grh), septate junctions (FasIII), and DAPI (Figures 4A–4D, data not shown). As expected at 3 dpi, the epithelium surrounding the control wound was composed of 35% polyploid nuclei with a DNA content of more than 2C (Figure 4E) (Losick et al., 2013, 2016). However, the epithelium-specific *Rok* knockdown did not significantly reduce the endocycle, as 37% of epithelial nuclei around the wound site were still polyploid with enlarged nuclei visible (Figures 4C and 4D). In the case of cell fusion, we noted that the *Rok* knockdown caused ectopic epithelial cell multinucleation (Figures 4A and 4B). There was a 3-fold increase in epithelial cells with two or more nuclei per cell even in the uninjured epithelium (Figure 4F). In total, 16% of the *Rok^{RNAi}* cells were multinucleated compared to only 5% in the control epithelium. As a result, we observed hyperfusion post injury as well, where *Rok^{RNAi}* syncytia were larger and more multinucleated (Figure 4G), even though the wound scar sizes were not statistically different than those of the controls (Figure 4H). In conclusion, we found that *Rok* is dispensable for WIP, both the endocycle and cell fusion.

We then investigated whether there was any defect in wound closure when *Rok* was knocked down. Re-epithelialization was assayed using epi-Gal4 expression of a membrane-linked red fluorescent protein (RFP; UAS-mCD8-RFP) (Bailey et al., 2020; Grendler et al., 2019). WIP promotes epithelial wound closure within 3 dpi when 94% of the wounds are closed for controls, whereas the WIP mutant (*E2F1^{RNAi} Rac^{DN}*) blocks both the endocycle and cell fusion and cannot heal (Figure 4I). However, there was no statistically significant difference between the percentage of wounds closed for the control and *Rok^{RNAi}* at 3 and 4 dpi, with 88% of *Rok^{RNAi}* wounds closing. This is consistent with our observations, and enlarged syncytia were also found not to impede wound closure in the *Drosophila* larval wound healing model (Wang et al., 2015). These findings show that NMII phosphorylation is dispensable for generation of the wound-induced polyploid cells and re-epithelialization.

Epithelial endocycling may serve to compensate for permanently severed abdominal muscle fibers

Given our findings that tension is elevated in healed, polyploid epithelium, we then sought to determine a possible mechanical function of this adaptation. The adult fly epithelium is not static but must conform with the movements of the fly abdominal cavity, which include stretching during female oogenesis and bending for male flies to copulate during mating (Aranha and Vasconcelos, 2018; Berthé and Lehmann, 2015; Kohatsu and Yamamoto, 2015). The epithelium is sandwiched between the external cuticle and abdominal muscle fibers, which run laterally across the ventral pleurite region studied herein. While the epithelium repairs by WIP from a puncture wound, the lateral muscle fibers remain permanently severed (Losick et al., 2013). We hypothesized that the observed increase in polyploid epithelial tension may serve to compensate for the lost muscle mechanics in the wounded abdominal area. To test this, we again measured the relative recoil velocity of Sqh-GFP in diploid epithelium in comparison to lateral muscle fiber tension using a muscle-specific Mhc-Tau-GFP strain to visualize the muscle cells (Figures 5A–5C and Video S4). Remarkably, we found that V_0 was on average 2-fold higher in the muscle as compared to the diploid epithelium (Figure 5C). This was a similar fold change in tension between the healed polyploid epithelium and uninjured diploid epithelium (Figures 2F and 3B).

To test whether epithelial WIP indeed functions to help compensate for lost muscle tension, we assayed whether WIP occurs in male flies and is required for abdominal bending. In male flies, a puncture wound also triggers formation of a giant syncytium, which fails to close when WIP is inhibited by blocking endocycle and cell fusion (Figures 5D and 5E). To test our hypothesis, we bilaterally injured male abdomens to permanently sever the lateral muscle fibers on both sides of a segment within the abdomen (Figures 5F and 5G). We then immobilized males and imaged their abdominal movements by quantifying the number of bends per minute (Figures 5H–5J and Video S5). A bend was defined as a male curling its abdomen from elongated to a 45° angle or greater curl, as measured from the midline axis of its body. Similar to copulation, the male flies vigorously curled their abdomens when pinned to a plate, and there was no significant difference between the ability of control flies to bend their abdomens in uninjured, diploid (–) epithelium compared to healed, polyploid epithelium (+) (Figure 5J). We then compared bending efficiency in male flies that cannot heal (*E2F1^{RNAi} Rac^{DN}*), cannot endocycle (*E2F1^{RNAi}*), or have reduced NMII phosphorylation (*Rok^{RNAi}*) before and after injury. There was no significant difference in the bending ability of uninjured fly strains except in *Rok^{RNAi}*, which we found has a reduced epithelial tension in diploid cells (Figures 3D and 5J and Video S5). The wounded (5 dpi) *Rok^{RNAi}* flies also had a reduced bending efficiency, which we attributed to a loss of tension in the surrounding diploid epithelium. However, when epithelial tension is only affected at the wound site, we found that there was a significant reduction in the bending frequency of both 5 dpi *E2F1^{RNAi} Rac^{DN}* and *E2F1^{RNAi}* males in comparison to their uninjured strains (Figure 5J and Video S5). Either an open wound or a healed epithelium that does not endoreplicate reduced bending efficiency. This suggests that the generation of polyploid cells, particularly by the endocycle, is necessary to restore abdominal bending in the fruit fly after injury.

Next, we tested whether the decrease in male abdominal bending efficiency could cause a defect in fertility by assaying for sperm transfer in the female lower reproductive tract, sperm storage organs. We generated a fly strain with Protamine B-GFP (ProtB-GFP), which labels the sperm head in epi-Gal4 background (Figure S3A) (Manier et al., 2010). Then we assayed whether there was a change in the percentage of females with GFP⁺ sperm in the sperm storage organs (spermatheca and seminal receptacle) at 24 h after mating (Figures S3A–S3C). However, we found that the males from the uninjured *E2F1^{RNAi} Rac^{DN}* strain had a sperm transfer defect, making it unfeasible to assay whether fertility was affected by a loss of WIP (Figure S3D). This strain background may interfere with the complex courtship behaviors required for mating (Ellendersen and von Philipsborn, 2017). Hence, this is why directly assessing fly abdominal movements is a more informative measure of WIP's effect on fly abdominal tissue. To examine this further, we assayed for changes in the angle of the male abdominal bend, and we were only able to detect slight changes in the degree of male abdominal bending between the uninjured and 5-dpi strains (Figure S3E). Overall, the increase in NMII via the endocycle is necessary to restore tissue movement and may serve a similar function in other organs where polyploid cells have been observed to arise.

DISCUSSION

There is now a growing list of adaptive roles for polyploidy in tissue repair and regeneration. The endocycle provides resistance to DNA damage and enables healing in the presence of genotoxic stress (Grendler et al., 2019; Hassel et al., 2014). In zebrafish epicardium, polyploid cells arise at the wound healing leading edge in response to mechanical tension to expedite the process of wound closure (Cao et al., 2017). In the mammalian liver and fly hindgut, polyploidy arises in response to injury and promotes resistance to tumorigenesis (Cohen et al., 2018; Wilkinson et al., 2019; Zhang et al., 2018). As a result, polyploidy has been suggested to be a treatment for cancer, as organ function does not appear to be perturbed by polyploidy (Lin et al., 2020). Here we present another advantage of polyploidy—namely, to enable a cell to adapt its mechanical properties to alter tissue tension.

The endocycle remodels the myosin network to alter tissue tension

The myosin network allows cells to adapt their shape, movement, and mechanics to facilitate cell- and tissue-level morphogenic events in development and regeneration (Heer and Martin, 2017; Zulueta-Coarasa and Fernandez-Gonzalez, 2017). In most wound healing models, the myosin network remodels at the epithelial leading edge into a cable (known as a purse string) to draw the edges of the wound closed (Wood et al., 2002; Zulueta-Coarasa and Fernandez-Gonzalez, 2017). Our results demonstrate that there is dramatic remodeling and induction of the epithelial NMII network in the context of WIP. However, we find a more uniform enrichment of NMII in wound-induced polyploid cells surrounding the wound scar with no obvious purse string formed during wound closure. In the uninjured adult fly epithelium, NMII appears polarized into a row-like structure with concentrated puncta throughout the meshwork. The puncta meshwork of the remodeled epithelium resembles the NMII organization seen during ventral furrow morphogenesis in the *Drosophila* embryo (Mason et al., 2013). These reorganizational changes occur concurrently with the endocycle and cell fusion, which simultaneously drives the changes in epithelial cell size and shape.

This is expected, as NMII is dynamic and studies in other systems have shown that organization is dictated by both cell and organism size constraints (Chanet et al., 2017; Gillard and Röper, 2020).

Regions of enriched NMII were found to be phosphorylated and under greater tension as determined by higher recoil velocities after laser ablation. However, this increased tension in polyploid cells was not dependent on myosin phosphorylation at least at Ser21, unlike the diploid epithelium. This is not the first time that tension has been found to occur independently of myosin phosphorylation. Studies have found a compensatory role of myosin crosslinking in force generation (Escuin et al., 2015; Ma et al., 2012; Sun et al., 2010). We plan to investigate this further using super-resolution microscopy, as the cytoskeletal network has yet to be characterized in giant, multinucleated polyploid cells. We also found that the endocycle, not cell fusion, was required for NMII upregulation, which was required for enhanced tension in the polyploid cells. The endocycle, unlike cell fusion, serves to restore lost synthetic capacity to the epithelium (Losick et al., 2016). Yet boosting the endocycle by *Myc* overexpression was not sufficient to boost NMII expression or epithelial tension. Therefore, we suspect that either the wound environment or a wound signal precedes the induction of NMII and the requirement for this mechanical change in the polyploid epithelium. One candidate is remodeling of the extracellular matrix (ECM), which is known to facilitate mechanical change (Martino et al., 2018). The polyploid cells form over the wound scar, where the cuticle has been permanently remodeled by the melanin plug, suggesting that ECM remodeling may be necessary to enhance epithelial tension (Losick et al., 2013).

Polyploidy enhances epithelial tension to restore *Drosophila* abdominal bending

Wound healing in adult *Drosophila* epithelium is triggered by a needle puncture wound that breaches the entire abdominal cavity, damaging the cuticle, epithelium, and muscle fibers. The adult fly abdominal epithelium is closely associated with lateral muscle fibers, which overlay this region of the ventral abdomen and are permanently severed as a result of injury (Losick et al., 2013, 2016). As such, the repaired abdomen has a permanently altered structure yet it maintains its organ function. The abdomen of the fruit fly needs to be able to stretch and bend in response to changing physiological and environmental conditions. Both male and female flies bend their abdomens during courtship behaviors (Aranha and Vasconcelos, 2018; Kohatsu and Yamamoto, 2015). Flies also rely on abdomen bending to shift their center of mass and counteract wing flapping to maneuver their flight (Berthé and Lehmann, 2015). Here we show that epithelial tension contributes to the male fly's ability to efficiently bend its abdomen. Reducing tension by *Rok^{RNAi}* in the uninjured diploid epithelium reduced male fly bending efficiency, demonstrating that epithelial tension is necessary for fly abdominal movements. In the *E2F1^{RNAi}* strain, the wound still closes by cell fusion but entry into the endocycle is inhibited, blocking NMII induction (Losick et al., 2013). This suggests that the endocycle acts, in part, to enable the repaired epithelium to adapt and change its tension to maintain abdominal movement when the tissue architecture is permanently altered by injury.

CONCLUSIONS

Many tissues lack a proliferative cell source (i.e., stem cell) and instead rely on polyploid cell growth as an alternative to cell proliferation to compensate for cell loss and restore tissue integrity (Gjelsvik et al., 2019; Lazzeri et al., 2019). Polyploid cells arise and persist with injury or age in many mammalian tissues, including cardiomyocytes in the heart, hepatocytes in the liver, tubule epithelial cells in the kidney, and cornea endothelial cells in the eye (Gjelsvik et al., 2019; Lazzeri et al., 2019). In the mammalian heart, cardiomyocyte differentiation from diploid to polyploid corresponds with increased mechanical output; but prior to our study, polyploid cell growth has yet to be tested as a source of mechanical change (Gan et al., 2020). In the fly, we find that WIP allows the epithelium to remodel its myosin network, which may compensate mechanically for the permanent loss of the injured abdominal muscle fibers. This may not be possible if the epithelial cells simply regenerated and replaced the same diploid epithelium. Thus, this study reveals that the generation of polyploid cells during wound repair may enable one cell type to mechanically compensate for the loss of another.

STAR★METHODS

RESOURCE AVAILABILITY

Lead contact—Further information and requests for resources and reagents should be directed to and will be fulfilled by the lead contact, Vicki Losick (vicki.losick@bc.edu).

Materials availability—This study did not generate new unique reagents.

Data and code availability—Microscopy data reported in this paper will be shared by the lead contact upon request.

This paper does not report original code.

Any additional information required to reanalyze the data reported in this paper is available from the lead contact upon request.

EXPERIMENTAL MODEL AND SUBJECT DETAILS

***Drosophila* husbandry and strains**—*Drosophila melanogaster* strains both female and male aged 7–9 days old were used in this study and reared on standard corn syrup soy food (Archon Scientific) at 25°C, 60% humidity, and 12h light/ dark cycle. The *Drosophila* strains used in this study are reported in Key Resources Table and acquired from either from Bloomington (b) and VDRC (v) stock center as indicated: GMR51F10-Gal4, referred to as epi-Gal4 (b38793), Sqh-GFP (b57144), Zip-GFP (b51564), ProtB-GFP (Manier et al., 2010), UAS-CD8.mRFP (b27392), *w¹¹¹⁸* (b3605), UAS-*Rok^{RNAi}* (b28797), UAS-*E2F1^{RNAi}* (v108837), UAS-*Rac^{DN}* (b6292), UAS-*ykt^{RNAi}* (v104523), and UAS-*Myc* (b9674). The control used for all studies, unless otherwise noted, was the epi-Gal4/*w¹¹¹⁸* strain.

METHOD DETAILS

Injury, dissection, and immunostaining—Adult flies were aged until 7–9 days old and then wounded and dissected as described (Bailey et al., 2020). Briefly, fixed abdomens were permeabilized in 1x PBS with 0.3% Triton X-100 and 0.3% BSA, then stained as indicated with primary antibodies: rabbit anti-GFP (Thermofisher, A-11122, AB_221569, 1:2000), mouse anti-FasIII (DSHB, 7G10, AB_528238, 1:50), rabbit anti-RFP (MBL, PM005, AB_591279, 1:1000), rabbit anti-Grh (AB_2568305, 1:300) (Losick et al., 2016), and rabbit anti-phospho-myosin (P-Myo, Cell Signaling #3671, AB_330248, 1:50). Secondary antibodies from Thermofisher included donkey anti-rabbit 488 (A21206, AB_2535792) and goat anti-mouse 568 (A11031, AB_144696) used at 1:1000 dilution. Stained abdomens were mounted in Vectashield on a glass coverslip and slide, with the inner tissue facing out.

Imaging and analysis—Tissue samples were imaged on a Zeiss Axiovert with ApoTome using a 20x or a 40x dry objective. Full Z stack images were taken at 0.5 μm per slice and flattened into a SUM of stacks projections using FIJI/ImageJ (SCR_002285) imaging software for all analysis. **Fluorescent Intensity** was measured for Sqh-GFP, Zip-GFP, and P-Myo protein expression. To do so, an ROI around the syncytium (using FasIII as a marker) or cells of interest were created and added to the ROI manager. If applicable, an ROI was also drawn around the wound site. For uninjured, diploid conditions, three ROI boxes were placed throughout the GFP or P-Myo channel to obtain an average staining intensity in the epithelium. For injured samples, the ROIs were placed within the syncytium, but not overlapping with wound scar, which has autofluorescence. The integrated density and area were measured using FIJI. Gray values were normalized to cell area to calculate the average fluorescence intensity. The fold change for each time post injury was calculated by dividing the normalized fluorescent intensity by its internal uninjured control. **Plot profiles** were generated using FIJI to visualize the spread of Sqh-GFP fluorescent intensity across a vertical line through the center of each image through the wound. Peaks in the two-dimensional graph correspond with greater fluorescent intensity and valleys correspond with lower fluorescent intensity and distance represents the distance of the vertical line from top to bottom of the images through the center of the wound. **Scar Sizes** were outlined and the areas were measured in FIJI.

Re-epithelialization was measured by scoring for the formation of a continuous epithelial sheet over the melanin scar. Abdomens expressing a membrane-bound UAS-mCD8-RFP under epi-Gal4 control were scored blind, as closed (wound scab covered with $< 20 \mu\text{m}$ diameter gaps) or open (uncovered wound scab, $> 20 \mu\text{m}$ diameter gaps).

Ploidy quantification was performed according to Bailey et al. (2020). Briefly, abdomens were stained with FasIII, Grh, and DAPI and the uninjured control epithelial nuclei were used as an internal control. All tissues were imaged under the same conditions and settings. Using FIJI, ROIs were drawn around each nucleus based on staining with the epithelial-specific nuclear marker Grh. ROIs were transferred to the corresponding DAPI SUM projection of the Z stack. The DAPI intensity and nuclear area were measured for each ROI, except for nuclei that overlapped with non-epithelial nuclei, which were excluded from analysis. The ploidy was calculated by normalizing the DAPI intensity of the average

value of the 2C uninjured epithelial nuclei for at least three abdomens per condition. The normalized ploidy values were binned into the indicated color-coded groups: 2C (0.6–2.9C), 4C (3.0–5.9C), 8C (6.0–12.9C), 16C (13.0–24.9C) and 32C (25–40C).

Cell Fusion was quantified by outlining the syncytia in FIJI using the FasIII cell-cell junctions as a guide and generating ROIs around nuclei stained for Grh. The number of nuclei per syncytium was recorded. In uninjured epithelium, the average number of mono- and multinucleated epithelial cells were quantified in $150 \times 150 \mu\text{m}$ tissue area.

Laser ablation was performed using either Nikon Eclipse microscope fitted to a WSU-CS1 Spinning disk and Andor technologies N₂ micropoint UV laser ablation system with 60x oil objective for Figures 2E–2H, 3A–3B, 5A–C and Video S1–S3 or Intelligent Imaging Innovations (3I) integrated Ablate module, Yokogawa spinning disk confocal on a Zeiss Axio Observer with 40x water objective for Figures 3C–3D. The laser ablation procedure was adapted from studies on *Drosophila* embryo (Fernandez-Gonzalez and Zallen, 2013; Martin et al., 2010). The micropoint was tuned to a 3–5 μm diameter in order to penetrate the thickness of the adult epithelium and ablate the Sqh-GFP epithelium with a single cut. To ablate a lateral muscle fiber, 2–3 cuts in a line were made to completely sever the Mhc-Tau-GFP expressing muscle cell. Whereas, a 1 μm diameter cut was sufficient to ablate targeted Sqh-GFP region with 3I Ablate module set to 70 out of 200 with 50 repetitions at laser power of 20%. Time-lapse images were recorded in both systems with a single plane to obtain the fastest frame rate. Laser ablation results in the recoil of the surrounding tissue whose initial velocity (V_0), calculated by displacement distance/ time, is proportional to the magnitude of the resting tension. Therefore, relative initial retraction velocities were compared for each sample and condition and correlated with relative tissue tension.

Rok inhibitor (γ -27632) was used to pharmacologically inhibit NMII activity as previously reported (Fernandez-Gonzalez and Zallen, 2013). Fly abdomens were treated *ex vivo* in buffer solution or buffer plus drug (50mM) solution for 10 minutes immediately upon dissection. For laser ablation studies, abdomens were then cut open and filleted onto a glass slide in a 50–50 Vectashield-halocarbon mixture. A coverslip was gently laid over the abdomens and immediately time-lapse imaged for laser ablation. For immunofluorescence, immediately following solution treatment, abdomens were dissected (cut, filleted, pinned) and fixed in 4% paraformaldehyde and later stained with antibodies as described above.

Fly Abdomen Bending analysis was performed on male flies, aged 10 days on date of scoring. Males that were subjected to bilateral injury, to disrupt the abdominal lateral muscle fibers, were allowed to recover for 5 days (5 dpi). Males were immobilized by securing them to a Sylgard dish by gently adhering their thorax to the dish with an insect pin. Males were video-recorded for 1min using SZX7 stereomicroscope with DP22 camera and Cellsense software (Olympus) and angle of each bend was measured in Fiji. A bend was defined as a male curling its abdomen from elongated straight to curled at 45 degree or greater angle as measured from the midline axis of its body, and then returning to its resting elongated position. Flies that did not move at all during imaging period were excluded from the analysis.

Sperm Transfer Assay was performed with male *Drosophila* carry the epi-Gal4, ProtB-GFP, in which sperm heads are labeled with GFP. Uninjured or 4dpi epi-Gal4, ProtB-GFP/*w¹¹¹⁸* and epi-Gal4, ProtB-GFP/UAS-*E2F1^{RNAi}* *Rac^{DN}* male flies were mated to virgin epi-Gal4 flies in ratio of 1:5. As in the bending assay, injured male flies were subjected to bilateral wound to disrupt the lateral muscle fibers. After 24h mating period, the female lower reproductive tracts were dissected, fixed, and mounted on glass slide using same conditions as described for the abdominal dissection. Sperm transfer was scored as positive if GFP-labeled sperm heads were detected in the female sperm storage organs (spermatheca and seminal receptacle).

QUANTIFICATION AND STATISTICAL ANALYSIS

All experiments were performed in triplicate with at least three biological replicates (fruit flies) measured and analyzed for each experiment. Excel was used for basic calculations (ex. fold change, displacement, initial velocity (V_0)) and statistical analysis was performed using Excel or GraphPad Prism (i.e., ANOVA, t tests with Welch's correction) as indicated in Figure Legend.

Supplementary Material

Refer to Web version on PubMed Central for supplementary material.

ACKNOWLEDGMENTS

We thank Kayla Gjeslvik who initiated this project and contributed to the experiments, analysis, and writing of this manuscript. For critical review of this manuscript, we thank members of the Losick laboratory (Dr. Erin Bailey, Rose Besen-McNally, Ari Dehn, Sara Kobielski, and John Park), Dr. Eric Folker, Dr. Greg Cox, Dr. Geoffrey Ganter, and Dr. Karissa Tilbury. We also thank Dr. Adam Martin and Soline Chanet (Massachusetts Institute of Technology) for assistance with the laser ablation assay and tension analysis. In addition, we thank the fly community, in particular the Bloomington *Drosophila* Stock Center (National Institutes of Health [NIH] grant P40-OD018537), the Developmental Studies Hybridoma Bank (created by the NIH Eunice Kennedy Shriver National Institute of Child Health and Human Development and maintained at the University of Iowa Department of Biology), the Vienna *Drosophila* Resource Center, and the Harvard Medical School TRiP Center (NIH National Institute of General Medical Sciences [NIGMS] grant R01-GM084947) for providing transgenic stocks or additional reagents used in this study. Images were acquired using the equipment of the MDI Biological Laboratory Light Microscopy Facility, which is supported by the Maine IDeA Network of Biomedical Research Excellence (NIH NIGMS grant GM103423), as well as from Bret Judson and the Boston College Imaging Core, which provided infrastructure and support. Research reported in this publication was supported by MDI Biological Laboratory, Boston College, and the NIH NIGMS (award R35-GM124691 to V.P.L. and Institutional Development Award P20-GM104318).

REFERENCES

- Aranha MM, and Vasconcelos ML (2018). Deciphering *Drosophila* female innate behaviors. *Curr. Opin. Neurobiol* 52, 139–148. [PubMed: 29940518]
- Bailey EC, Dehn AS, Gjeslvik KJ, Besen-McNally R, and Losick VP (2020). A *Drosophila* model to study wound-induced polyploidization. *J. Vis. Exp* 160, 10.3791/61252.
- Berthé R, and Lehmann FO (2015). Body appendages fine-tune posture and moments in freely manoeuvring fruit flies. *J. Exp. Biol* 218, 3295–3307. [PubMed: 26347566]
- Besen-McNally R, Gjeslvik KJ, and Losick VP (2021). Wound-induced polyploidization is dependent on integrin-Yki signaling. *Biol. Open* 10, bio055996. [PubMed: 33355119]
- Cao J, Wang J, Jackman CP, Cox AH, Trembley MA, Balowski JJ, Cox BD, De Simone A, Dickson AL, Di Talia S, et al. (2017). Tension creates an endoreplication wavefront that leads regeneration of epicardial tissue. *Dev. Cell* 42, 600–615.e4. [PubMed: 28950101]

- Chanet S, Miller CJ, Vaishnav ED, Ermentrout B, Davidson LA, and Martin AC (2017). Actomyosin meshwork mechanosensing enables tissue shape to orient cell force. *Nat. Commun* 8, 15014. [PubMed: 28504247]
- Cohen E, Allen SR, Sawyer JK, and Fox DT (2018). Fizzy-related dictates A cell cycle switch during organ repair and tissue growth responses in the *Drosophila* hindgut. *eLife* 7, e38327. [PubMed: 30117808]
- Ellenderson BE, and von Philipsborn AC (2017). Neuronal modulation of *D. melanogaster* sexual behaviour. *Curr. Opin. Insect Sci* 24, 21–28. [PubMed: 29208219]
- Escuin S, Vernay B, Savery D, Gurniak CB, Witke W, Greene ND, and Copp AJ (2015). Rho-kinase-dependent actin turnover and actomyosin disassembly are necessary for mouse spinal neural tube closure. *J. Cell Sci* 128, 2468–2481. [PubMed: 26040287]
- Fernandez-Gonzalez R, and Zallen JA (2013). Wounded cells drive rapid epidermal repair in the early *Drosophila* embryo. *Mol. Biol. Cell* 24, 3227–3237. [PubMed: 23985320]
- Fox DT, and Duronio RJ (2013). Endoreplication and polyploidy: insights into development and disease. *Development* 140, 3–12. [PubMed: 23222436]
- Frawley LE, and Orr-Weaver TL (2015). Polyploidy. *Curr. Biol* 25, R353–R358. [PubMed: 25942544]
- Fujiwara T, Bandi M, Nitta M, Ivanova EV, Bronson RT, and Pellman D (2005). Cytokinesis failure generating tetraploids promotes tumorigenesis in p53-null cells. *Nature* 437, 1043–1047. [PubMed: 16222300]
- Gan P, Patterson M, and Sucov HM (2020). Cardiomyocyte polyploidy and implications for heart regeneration. *Annu. Rev. Physiol* 82, 45–61. [PubMed: 31585517]
- Gillard G, and Röper K (2020). Control of cell shape during epithelial morphogenesis: recent advances. *Curr. Opin. Genet. Dev* 63, 1–8. [PubMed: 32092616]
- Gjelsvik KJ, Besen-McNally R, and Losick VP (2019). Solving the polyploid mystery in health and disease. *Trends Genet.* 35, 6–14. [PubMed: 30470486]
- González-Rosa JM, Sharpe M, Field D, Soonpaa MH, Field LJ, Burns CE, and Burns CG (2018). Myocardial polyploidization creates a barrier to heart regeneration in zebrafish. *Dev. Cell* 44, 433–446.e7. [PubMed: 29486195]
- Grendler J, Lowgren S, Mills M, and Losick VP (2019). Wound-induced polyploidization is driven by Myc and supports tissue repair in the presence of DNA damage. *Development* 146, dev173005. [PubMed: 31315896]
- Han L, Choudhury S, Mich-Basso JD, Ammanamanchi N, Ganapathy B, Suresh S, Khaladkar M, Singh J, Maehr R, Zuppo DA, et al. (2020). Lamin B2 levels regulate polyploidization of cardiomyocyte nuclei and myocardial regeneration. *Dev. Cell* 53, 42–59.e11. [PubMed: 32109383]
- Harrison BD, Hashemi J, Bibi M, Pulver R, Bavli D, Nahmias Y, Wellington M, Sapiro G, and Berman J (2014). A tetraploid intermediate precedes aneuploid formation in yeasts exposed to fluconazole. *PLoS Biol.* 12, e1001815. [PubMed: 24642609]
- Hassel C, Zhang B, Dixon M, and Calvi BR (2014). Induction of endocycles represses apoptosis independently of differentiation and predisposes cells to genome instability. *Development* 141, 112–123. [PubMed: 24284207]
- Heer NC, and Martin AC (2017). Tension, contraction and tissue morphogenesis. *Development* 144, 4249–4260. [PubMed: 29183938]
- Jiang J, Woulfe DS, and Papoutsakis ET (2014). Shear enhances thrombopoiesis and formation of microparticles that induce megakaryocytic differentiation of stem cells. *Blood* 124, 2094–2103. [PubMed: 24948658]
- Kim JH, Ren Y, Ng WP, Li S, Son S, Kee YS, Zhang S, Zhang G, Fletcher DA, Robinson DN, and Chen EH (2015). Mechanical tension drives cell membrane fusion. *Dev. Cell* 32, 561–573. [PubMed: 25684354]
- Kohatsu S, and Yamamoto D (2015). Visually induced initiation of *Drosophila* innate courtship-like following pursuit is mediated by central excitatory state. *Nat. Commun* 6, 6457. [PubMed: 25743851]
- Lazzeri E, Angelotti ML, Peired A, Conte C, Marschner JA, Maggi L, Mazzinghi B, Lombardi D, Melica ME, Nardi S, et al. (2018). Endocycle-related tubular cell hypertrophy and progenitor

proliferation recover renal function after acute kidney injury. *Nat. Commun* 9, 1344. [PubMed: 29632300]

- Lazzeri E, Angelotti ML, Conte C, Anders HJ, and Romagnani P (2019). Surviving acute organ failure: cell polyploidization and progenitor proliferation. *Trends Mol. Med* 25, 366–381. [PubMed: 30935780]
- Lin YH, Zhang S, Zhu M, Lu T, Chen K, Wen Z, Wang S, Xiao G, Luo D, Jia Y, et al. (2020). Mice with increased numbers of polyploid hepatocytes maintain regenerative capacity but develop fewer hepatocellular carcinomas following chronic liver injury. *Gastroenterology* 158, 1698–1712. [PubMed: 31972235]
- Losick VP, Fox DT, and Spradling AC (2013). Polyploidization and cell fusion contribute to wound healing in the adult *Drosophila* epithelium. *Curr. Biol* 23, 2224–2232. [PubMed: 24184101]
- Losick VP, Jun AS, and Spradling AC (2016). Wound-induced polyploidization: regulation by Hippo and JNK signaling and conservation in mammals. *PLoS One* 11, e0151251. [PubMed: 26958853]
- Lye CM, and Sanson B (2011). Tension and epithelial morphogenesis in *Drosophila* early embryos. *Curr. Top. Dev. Biol* 95, 145–187. [PubMed: 21501751]
- Ma X, Kovács M, Conti MA, Wang A, Zhang Y, Sellers JR, and Adelstein RS (2012). Nonmuscle myosin II exerts tension but does not translocate actin in vertebrate cytokinesis. *Proc. Natl. Acad. Sci. USA* 109, 4509–4514. [PubMed: 22393000]
- Manier MK, Belote JM, Berben KS, Novikov D, Stuart WT, and Pitnick S (2010). Resolving mechanisms of competitive fertilization success in *Drosophila melanogaster*. *Science* 328, 354–357. [PubMed: 20299550]
- Martin AC, Gelbart M, Fernandez-Gonzalez R, Kaschube M, and Wieschaus EF (2010). Integration of contractile forces during tissue invagination. *J. Cell Biol* 188, 735–749. [PubMed: 20194639]
- Martino F, Perestrelo AR, Vinarský V, Pagliari S, and Forte G (2018). Cellular mechanotransduction: from tension to function. *Front. Physiol* 9, 824. [PubMed: 30026699]
- Mason FM, Tworoger M, and Martin AC (2013). Apical domain polarization localizes actin-myosin activity to drive ratchet-like apical constriction. *Nat. Cell Biol* 15, 926–936. [PubMed: 23831726]
- Orr-Weaver TL (2015). When bigger is better: the role of polyploidy in organogenesis. *Trends Genet.* 31, 307–315. [PubMed: 25921783]
- Patterson M, Barske L, Van Handel B, Rau CD, Gan P, Sharma A, Parikh S, Denholtz M, Huang Y, Yamaguchi Y, et al. (2017). Frequency of mononuclear diploid cardiomyocytes underlies natural variation in heart regeneration. *Nat. Genet* 49, 1346–1353. [PubMed: 28783163]
- Qi F, and Zhang F (2020). Cell cycle regulation in the plant response to stress. *Front. Plant Sci* 10, 1765. [PubMed: 32082337]
- Sellers JR, Eisenberg E, and Adelstein RS (1982). The binding of smooth muscle heavy meromyosin to actin in the presence of ATP. Effect of phosphorylation. *J. Biol. Chem* 257, 13880–13883. [PubMed: 6128340]
- Shu Z, Row S, and Deng WM (2018). Endoreplication: the good, the bad, and the ugly. *Trends Cell Biol.* 28, 465–474. [PubMed: 29567370]
- Storchova Z (2014). Ploidy changes and genome stability in yeast. *Yeast* 31, 421–430. [PubMed: 25155743]
- Sun SX, Walcott S, and Wolgemuth CW (2010). Cytoskeletal cross-linking and bundling in motor-independent contraction. *Curr. Biol* 20, R649–R654. [PubMed: 20692617]
- Tamori Y, and Deng WM (2013). Tissue repair through cell competition and compensatory cellular hypertrophy in postmitotic epithelia. *Dev. Cell* 25, 350–363. [PubMed: 23685249]
- Todd RT, Forche A, and Selmecki A (2017). Ploidy variation in fungi: polyploidy, aneuploidy, and genome evolution. *Microbiol. Spectr* 5, 5.4.09.
- Uehata M, Ishizaki T, Satoh H, Ono T, Kawahara T, Morishita T, Tamakawa H, Yamagami K, Inui J, Maekawa M, and Narumiya S (1997). Calcium sensitization of smooth muscle mediated by a Rho-associated protein kinase in hypertension. *Nature* 389, 990–994. [PubMed: 9353125]
- Uroz M, Garcia-Puig A, Tekeli I, Elosegui-Artola A, Abenza JF, Marín-Llauradó A, Pujals S, Conte V, Albertazzi L, Roca-Cusachs P, et al. (2019). Traction forces at the cytotkinetic ring regulate cell division and polyploidy in the migrating zebrafish epicardium. *Nat. Mater* 18, 1015–1023. [PubMed: 31160803]

- Vasquez CG, Tworoger M, and Martin AC (2014). Dynamic myosin phosphorylation regulates contractile pulses and tissue integrity during epithelial morphogenesis. *J. Cell Biol* 206, 435–450. [PubMed: 25092658]
- Wang Y, Antunes M, Anderson AE, Kadrmas JL, Jacinto A, and Galko MJ (2015). Integrin adhesions suppress syncytium formation in the *Drosophila* larval epidermis. *Curr. Biol* 25, 2215–2227. [PubMed: 26255846]
- Wilkinson PD, Delgado ER, Alencastro F, Leek MP, Roy N, Weirich MP, Stahl EC, Otero PA, Chen MI, Brown WK, and Duncan AW (2019). The polyploid state restricts hepatocyte proliferation and liver regeneration in mice. *Hepatology* 69, 1242–1258. [PubMed: 30244478]
- Wood W, Jacinto A, Grose R, Woolner S, Gale J, Wilson C, and Martin P (2002). Wound healing recapitulates morphogenesis in *Drosophila* embryos. *Nat. Cell Biol* 4, 907–912. [PubMed: 12402048]
- Xiang J, Bandura J, Zhang P, Jin Y, Reuter H, and Edgar BA (2017). EGFR-dependent TOR-independent endocycles support *Drosophila* gut epithelial regeneration. *Nat. Commun* 8, 15125. [PubMed: 28485389]
- Zhang S, Zhou K, Luo X, Li L, Tu HC, Sehgal A, Nguyen LH, Zhang Y, Gopal P, Tarlow BD, et al. (2018). The polyploid state plays a tumor-suppressive role in the liver. *Dev. Cell* 44, 447–459.e5. [PubMed: 29429824]
- Zulueta-Coarasa T, and Fernandez-Gonzalez R (2017). Tension (re)builds: biophysical mechanisms of embryonic wound repair. *Mech. Dev* 144 (Pt A), 43–52. [PubMed: 27989746]

Highlights

- The endocycle upregulates NMII during wound healing
- The endocycle is required, but not sufficient, to enhance epithelial tension after wound repair
- Loss of epithelial tension impairs fly abdominal bending

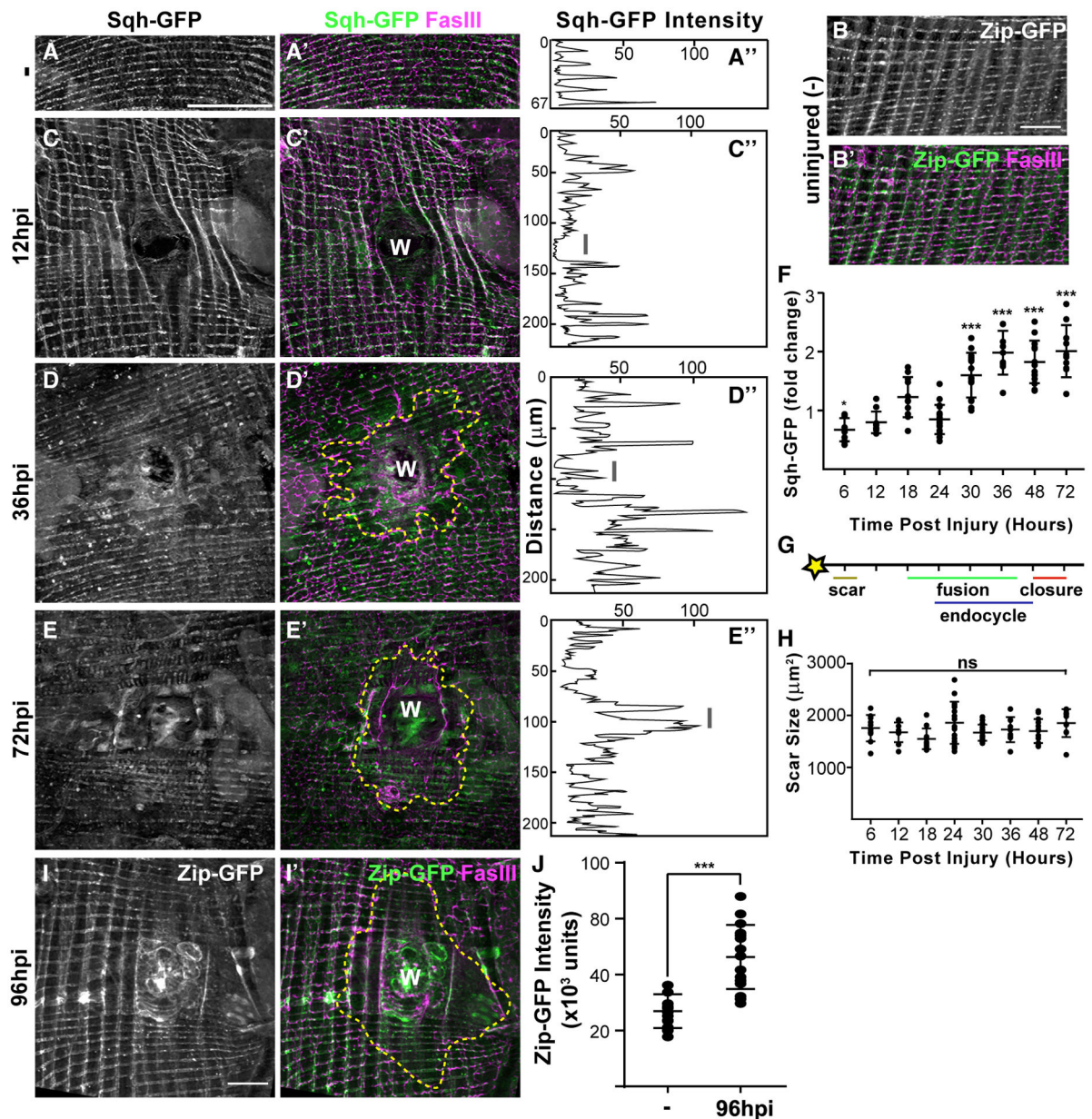


Figure 1. Nonmuscle myosin II is upregulated and persists in wound-induced polyloid cells (A–E and I to A’–E’ and I’) Localization and expression of the nonmuscle myosin II regulatory light chain (Sqh-GFP) and heavy chain (Zip-GFP) in uninjured adult *Drosophila* abdominal epithelium (A, A’, B, and B’’) and during wound healing (C–E, C’–E’, I, and I’). Representative immunofluorescent images are shown of the uninjured (–) or indicated time in hours post injury (hpi). Merged images show GFP (green) and FasIII septate junction (magenta). The giant polyloid syncytium (dashed yellow line) begins to form by 36 hpi to repair epithelium and cover the wound scar (W) by 72 hpi. Scale bars, 50 μm. (A’’–E’’) Plot profiles depict the range of the relative Sqh-GFP intensity through the representative images. The gray line is the wound scar site and distance represents the vertical profile (top to bottom through the center of the image).

(F) Quantification of fold-change Sqh-GFP intensity at 6 (n = 10), 12 (n = 10), 18 (n = 11), 24 (n = 17), 30 (n = 15), 36 (n = 9), 48 (n = 15), and 72 (n = 10) hpi for individual flies. Data represent the mean \pm SD with one-way ANOVA with Dunnett's multiple comparisons test. ns, not significant ($p > 0.05$). * $p = 0.0457$ and *** $p < 0.001$.

(G) Timeline of wound healing events: injury (star, 0 hpi), scar formation (1–6 hpi), cell fusion (18–48 hpi), endocycle (24–48 hpi), and closure (48–72 hpi). The tickmarks align with time post injury in (F).

(H) Quantification of wound scar sizes. Data represent the mean \pm SD with two-way ANOVA with Tukey's multiple comparisons test.

(J) Quantification of Zip-GFP intensity of uninjured (n = 15) and 96-hpi (n = 17) flies. Data represent the mean \pm SD with the unpaired two-tailed t test with Welch's correction. *** $p < 0.001$.

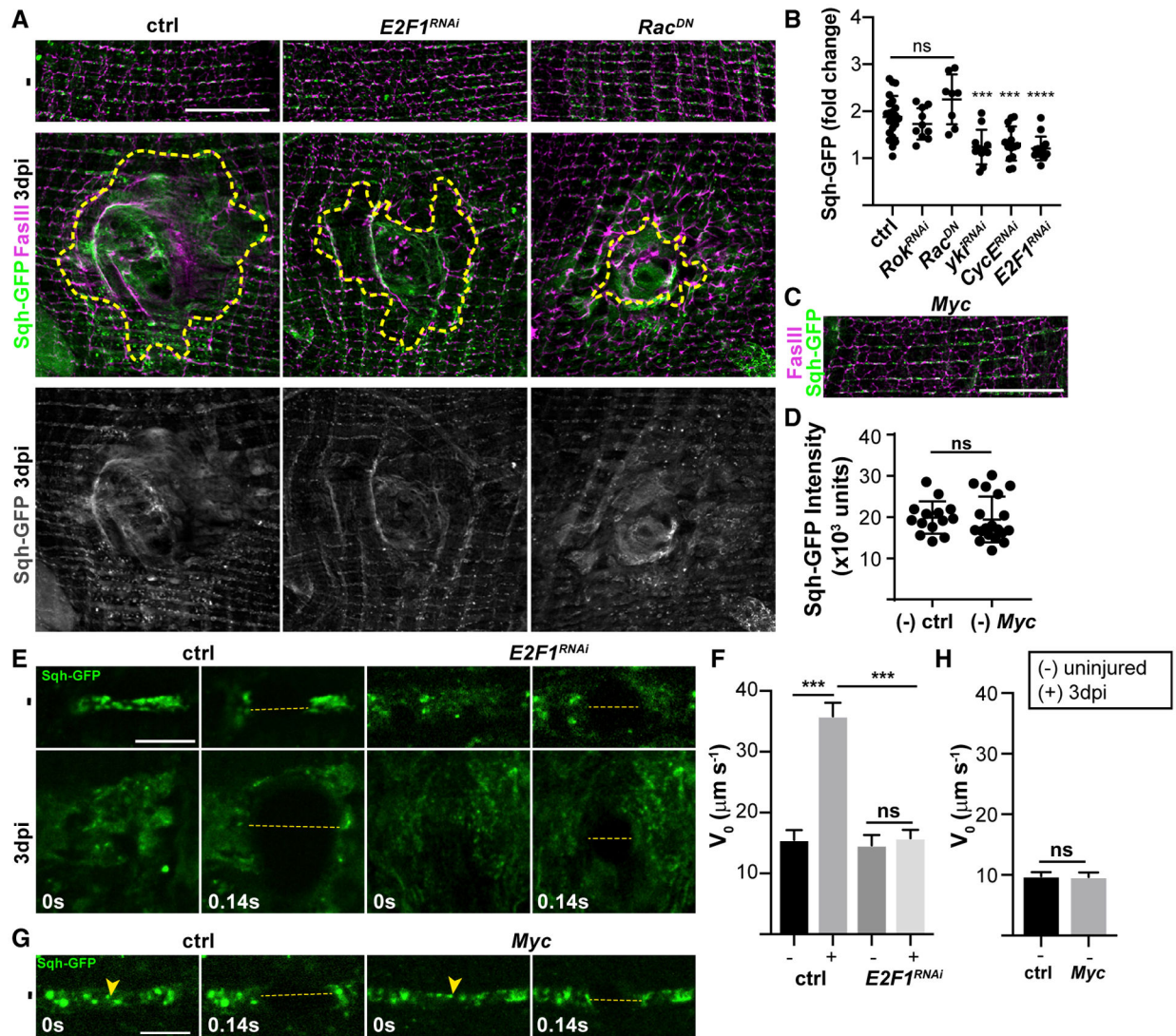


Figure 2. The endocycle is required, but not sufficient, to enhance NMII expression and epithelial tension

(A) Representative immunofluorescent images of Sqh-GFP (green [top] or white [bottom]) and FasIII (magenta) from the uninjured (-) or 3 dpi fly in the control, *E2F1^{RNAi}* (blocks endocycle), and *Rac^{DN}* (reduces cell fusion). Syncytium is indicated by the dashed yellow line. Scale bar, 50 μm .

(B) Quantification of fold change in Sqh-GFP expression at 3 dpi in the control (n = 22), *yki^{RNAi}* (n = 11), *CycE^{RNAi}* (n = 14), *E2F1^{RNAi}* (n = 14), and *Rac^{DN}* (n = 8). Data represent the mean \pm SD with one-way ANOVA with Tukey's multiple comparisons test. ns, not significant ($p > 0.05$). *** $p < 0.001$.

(C) Immunofluorescence image of epithelium overexpressing *Myc*, an endoreplication inducer (Grendler et al., 2019). Scale bar, 50 μm .

(D) Quantification of Sqh-GFP intensity in uninjured (-), control (n = 9), and *Myc* (n = 19) strains. Data represent the mean \pm SD with the unpaired two-tailed t test.

(E) Images of Sqh-GFP in the frame before (0 s) and after (0.14 s) laser ablation of the adult fly abdomen from control and *E2FI^{RNAi}*. Scale bar, 10 μm . Laser ablation cut site (arrowhead) and recoil distance (dashed yellow lines).

(F) Quantification of the initial retraction velocity (in $\mu\text{m/s}$) of uninjured (–) (n = 13) and 3 dpi (n = 12) strains and *E2FI^{RNAi}* uninjured (–) (n = 11) and 3 dpi (n = 13) strains. Data represent the mean \pm SD with one-way ANOVA with Sidak's multiple comparisons test. ***p < 0.001.

(G) Images of Sqh-GFP from the frame before (0 s) and after (0.14 s) laser ablation in control and *Myc* flies. Scale bar, 10 μm .

(H) Quantification of the initial retraction velocity (in $\mu\text{m/s}$) of uninjured strains (control, n = 13; and *Myc*, n = 11). Data represent the mean \pm SD with the unpaired two-tailed t test with Welch's correction. See Figure S1 and Videos S1 and S2.

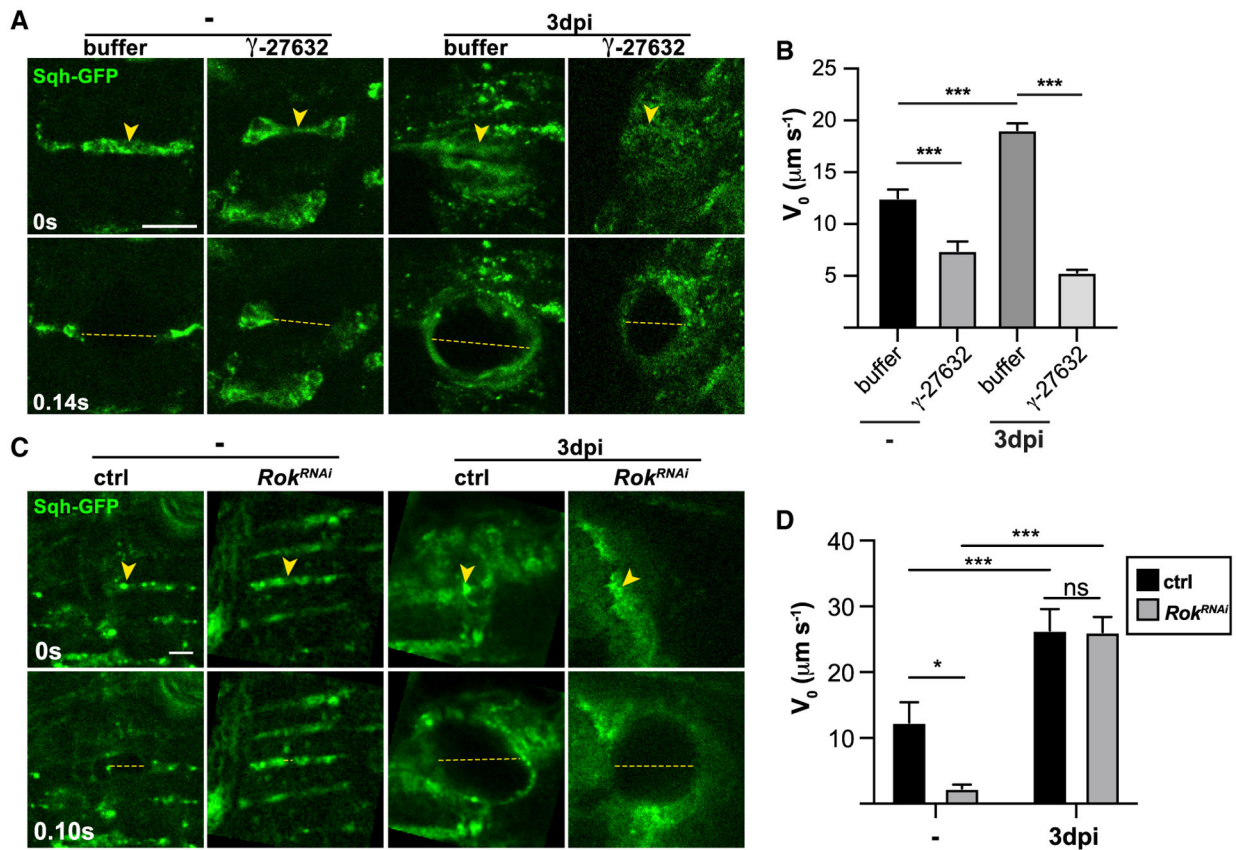


Figure 3. Myosin phosphorylation by Rok is required for tension in uninjured diploid but not polyploid epithelium

(A) Images of Sqh-GFP in the frame before (0 s) and after (0.14 s) laser ablation in the adult fly abdomen. Tissues were treated with buffer or Rok inhibitor (γ -27632, 50 mM) prior to ablation. Scale bar, 10 μm .

(B) Quantification of the initial retraction velocity of uninjured (–) epithelium (buffer, $n = 8$; and γ -27632, $n = 8$) and 3 dpi epithelium (buffer, $n = 6$; and γ -27632, $n = 8$). Data represent the mean \pm SE with one-way ANOVA with Tukey’s multiple comparisons test. *** $p < 0.001$.

(C) Images of Sqh-GFP in the frame before (0 s) and after (0.10 s) laser ablation in the control or Rok^{RNAi} strain. Scale bar, 5 μm .

(D) Quantification of the initial retraction velocity of the uninjured epithelium (control, $n = 10$; and Rok^{RNAi} , $n = 11$) and 3 dpi epithelium (control, $n = 7$; and Rok^{RNAi} , $n = 8$). Data represent the mean \pm SE with two-way ANOVA with Sidak’s multiple comparisons test. * $p < 0.05$ and *** $p < 0.001$. Laser ablation cut site (arrowhead) and recoil distance (dashed yellow lines). See Video S3.

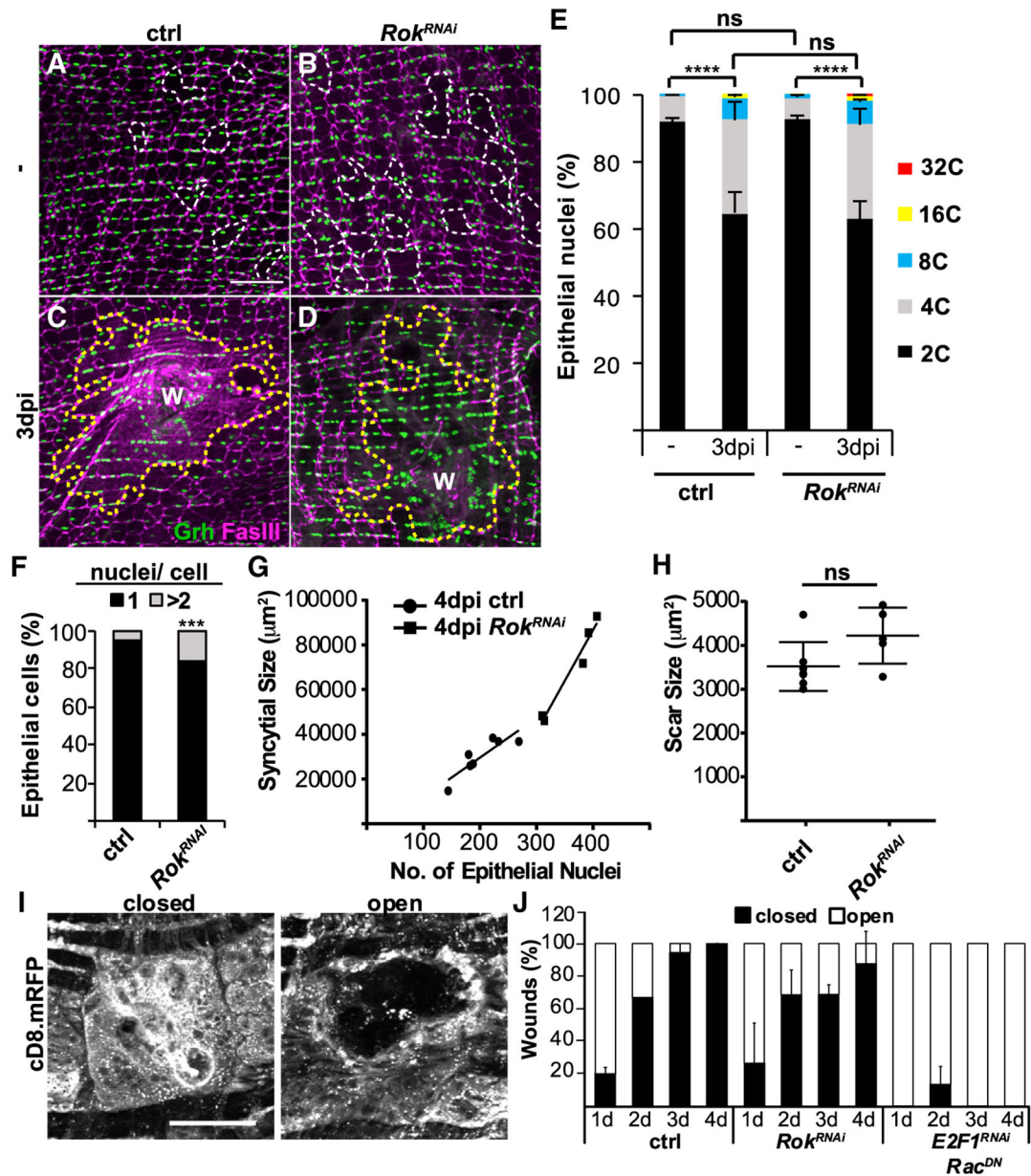


Figure 4. Rok is not required for WIP

(A–D) Immunofluorescence images of uninjured (–) and 3 dpi fly epithelium in the control (A and C) and *Rok^{RNAi}* (B and D). Epithelial nuclei (Grh, green), septate junctions (FasIII, magenta), giant syncytium (dashed yellow line), and multinucleated cells are outlined (white dashed line) and the wound scar (W) is shown. Scale bar, 50 μ m.

(E) Quantification of epithelial ploidy from control (uninjured, n = 7; and 3 dpi, n = 4) and *Rok^{RNAi}* (uninjured, n = 5; and 3 dpi, n = 4). Data represent the mean \pm SD with two-way ANOVA with Tukey’s multiple comparisons test. ns, not significant ($p > 0.05$). **** $p < 0.0001$.

(F) *Rok^{RNAi}* enhances epithelial cell size and multinucleation. Quantification of epithelial nuclear number per cell in control (n = 6) and *Rok^{RNAi}* (n = 6) epithelium from uninjured flies. Data represent the mean \pm SE with two-tailed unpaired t test. **p < 0.01.

(G) Quantification of 3-dpi epithelial syncytium size and number of epithelial nuclei for control and *Rok^{RNAi}* strains.

(H) Quantification of wound scar size for control (n = 7) and *Rok^{RNAi}* (n = 5) strains. Data represent the mean \pm SD with two-tailed unpaired t test with Welch's correction.

(I) Representative immunofluorescent images for re-epithelization as detected by expression of membrane-linked RFP (epi-Gal4, UAS-mCD8-RFP) at 3 dpi. Scale bar, 20 μ m.

(J) Wound closure was scored as open (> 20- μ m gap in mCD8-RFP epithelium) for the control (1 dpi, n = 15; 2 dpi, n = 15; 3 dpi, n = 18; and 4 dpi, n = 14), *Rok^{RNAi}* (1 dpi, n = 19; 2 dpi, n = 19; 3 dpi, n = 16; and 4 dpi, n = 16), and *E2F1^{RNAi} Rac^{DN}* (1 dpi, n = 16; 2 dpi, n = 15; 3 dpi, n = 16; and 4 dpi, n = 7). Data represent the mean \pm SD with two-way ANOVA with Tukey's multiple comparisons test.

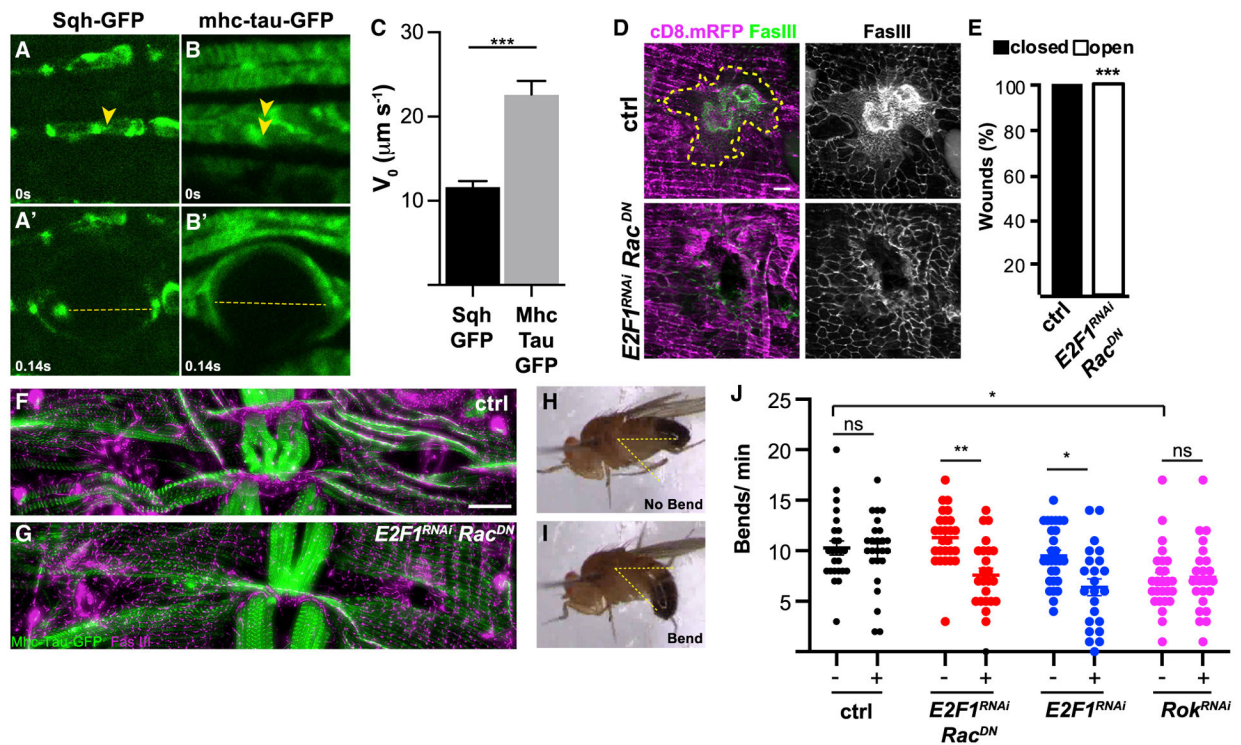


Figure 5. WIP restores male fly bending efficiency post injury

(A–B') Images of the frame before (0 s; A and B) and after (0.14 s; A' and B') laser ablation of the adult fly abdominal (A and A') epithelial Sqh-GFP and (B and B') lateral muscle fiber labeled by Mhc-Tau-GFP. Scale bar, 10 μm . Laser ablation cut site (arrowhead) and recoil distance (dashed yellow lines).

(C) Quantification of the initial retraction velocity of Sqh-GFP ($n = 17$) and mhc-tau-GFP ($n = 15$). Data represent the mean \pm SE with the unpaired t test with Welch's correction. *** $p < 0.001$.

(D) Representative immunofluorescent images for control and $E2F1^{RNAi} Rac^{DN}$ males at 4 dpi. The yellow dashed line outlines the syncytium. Scale bar, 50 μm .

(E) Wound closure was scored as open ($> 20\text{-}\mu\text{m}$ gap in mCD8-RFP epithelium) for the control ($n = 10$) and $E2F1^{RNAi} Rac^{DN}$ ($n = 9$). Percentages of closed wounds were calculated and data were analyzed by Fisher's exact test.

(F and G) Representative immunofluorescent images of a bilaterally wounded male at 5 dpi. Images show permanently severed muscle after injury for the control (F) and $E2F1^{RNAi} Rac^{DN}$ (no WIP) (G). FasIII (magenta) and Mhc-Tau-GFP (green). Scale bar, 50 μm .

(H and I) Representative image of a male fly not bending its abdomen (H) and bending its abdomen (I).

(J) Quantification of abdominal bending males fly strains that were uninjured (–) or at 5 dpi (+), respectively: control ($n = 25$ and 25), $E2F1^{RNAi} Rac^{DN}$ ($n = 26$ and 24), $E2F1^{RNAi}$ ($n = 28$ and 23), and Rok^{RNAi} ($n = 25$ and 23). Data represent the mean \pm SE with two-way ANOVA with Tukey's multiple comparisons test. ns, not significant ($p > 0.05$). * $p < 0.05$ and ** $p < 0.01$. See Video S5.

KEY RESOURCES TABLE

| REAGENT or RESOURCE | SOURCE | IDENTIFIER |
|--|----------------------|------------------------------|
| Antibodies | | |
| Mouse anti-FasIII | DSHB | Cat#7G10; RRID: AB_528238 |
| Rabbit anti-RFP | MBL | Cat#PM005; RRID: AB_591279 |
| Rabbit anti-Grh | Losick et al. (2016) | RRID: AB_2568305 |
| Rabbit anti-Phospho-Myosin | Cell Signaling | Cat#3671; RRID: AB_330248 |
| Donkey anti-Rabbit 488 | ThermoFisher | Cat#A21206; RRID: AB_2535792 |
| Goat anti-Mouse 568 | ThermoFisher | Cat#A11031; RRID: AB_144696 |
| Rabbit anti-GFP | ThermoFisher | Cat#A11122; RRID: AB_221569 |
| Chemicals, peptides, and recombinant proteins | | |
| Rok inhibitor (Y-27632) | Sigma | Cat#Y0503 |
| Experimental models: Organisms/strains | | |
| Sqh-GFP (y[1] w[*] cv[1] sqh[AX3]; P{w[+mC] = sqh-GFP.RLC}2) | BDSC | Cat#57144 |
| Zip-GFP (w[*]; P{w[+mC] = PTT-GC}zip[CC01626]/SM6a) | BDSC | Cat#51564 |
| UAS-mCD8.ChRFP (w[*]; P{w[+mC] = UAS-mCD8.ChRFP}3) | BDSC | Cat#27392 |
| w[1118] | BDSC | Cat#3605 |
| UAS-RokRNAi (y[1] v[1]; P{y[+t7.7] v[+t1.8] = TRiP.JF03225}attP2) | BDSC | Cat#28797 |
| UAS-RacDN (y[1] w[*]; P{w[+mC] = UAS-Rac1.N17}1) | BDSC | Cat#6292 |
| UAS-Myc (w[1118]; P{w[+mC] = UAS-Myc.Z}132) | BDSC | Cat#9674 |
| UAS-ykiRNAi (P{KK109756}VIE-260B) | VDRC | Cat#104523 |
| UAS-E2F1RNAi (P{KK100304}VIE-260B) | VDRC | Cat#108837 |
| ProtB-GFP (w[*]; P{w[+mC] = protamineB-eGFP}2/CyO) | Manier et al. (2010) | |
| epi-Gal4 (w[1118]; P{y[+t7.7] w[+mC] = GMR51F10-GAL4}attP2GMR51F10-Gal4) | BDSC | Cat#38793 |
| Software and algorithms | | |
| GraphPad Prism | | RRID: SCR_002798 |
| Fiji/ImageJ | | RRID: SCR_002285 |